IEEE Robotics and Automation Letters (RA-L) paper, presented at ICRA 2026, Vienna, Austria. Cite as RA-L paper.

Soft 3D-Printed Endoskeleton for Precise Tendon Routing in Soft Robotics

Emanuele Solfiti, Alessio Mondini, Emanuela Del Dottore, *Member, IEEE*, Barbara Mazzolai, *Member, IEEE*, and Alberto Parmiggiani

***Abstract*—This paper presents the design, development, and testing of a soft 3D-printed endoskeleton for arbitrary cable routing in tendon-driven soft actuators. The endoskeleton is embedded in a silicone body, and it is fixed to the mold prior to the casting process. It enables tendons to be placed through predefined eyelets, ensuring accurate positioning within the soft body. To minimize its impact on the overall stiffness of the soft body, the endoskeleton was designed with a slim profile, flexible connections, and 3D-printed with elastic material (Shore A hardness 50), selected to roughly match the mechanical properties of the surrounding silicone matrix (typically with Shore 00 hardness 20–30). Key features of the proposed solution include a 3D-printable guide for tendon routing that is (1) fully soft, (2) easy to place, (3) rapidly reconfigurable for arbitrary tendon paths, (4) adaptable to variable soft body geometries, and (5) easy to fabricate with single-step casting. The current work describes the design, manufacturing, simulation, and testing of a simplified case study in which the endoskeleton is employed to reproduce a target pose predicted by FE analysis with good matching, demonstrating the effectiveness of the approach.**

***Index Terms*—Soft robot materials and design, tendon/wire mechanism, soft sensors and actuators.**

I. Introduction

SOFT robotics aims to leverage the flexibility and adaptability of soft materials, most commonly polymers like urethanes or silicones, to create robots capable of complex, delicate, and possibly intrinsically safe interactions with their surroundings [1], [2]. Additional rigid, flexible, or liquid elements can be incorporated into the soft bodies to gain sensing or actuation functionalities [3]. Among the various actuation mechanisms in soft robotics, tendon-driven actuators stand out for their ability to mimic the natural movement drivers of biological systems. Motor-tendon coupling transmits forces, enabling control over the bending and twisting of soft robotic structures. However, enclosing tendons in polymeric matrices, especially when involving casting procedures, presents several technical challenges [4]. The primary issues include maintaining the body's structural softness, integrity, and durability, ensuring smooth and frictionless movement within the soft material matrix, and preventing wear and tear over repeated actuation cycles. Additionally, the encapsulation process must ensure that the tendon remains in the desired position during casting, accounting for possible buoyancy and drag effects to preserve the accuracy and reliability of the actuator's expected behaviors.

This paper presents a method for accurately placing tendons in soft robotic bodies. The approach is particularly convenient when the path of the tendon is not straight but develops as a continuous curve in the 3D domain. Nonlinear tendon arrangements can, for example, be desired to enable shape-shifting [5], twisting without buckling [6], coiling [7], [8], and to enhance functionalities (e.g., out of plane movements) in grippers, manipulators, or locomotion systems with actuators having irregular, cylindrical, or conical shapes.

Current approaches usually introduce stiff supports, like rigid tubes or ad hoc shapes, arranged along the tendon path into the body at discrete positions [5], [7], [8], [9], [10] or winding the tendons around grooves [6]. However, these solutions require placing several separate components, which is time-consuming and prone to errors. At the same time, the stiff parts can compromise the softness and maneuverability of the developed robot and can delaminate easily from the body structure due to the high difference in stiffness.

In addition, they typically require a multi-step casting procedure, for example, to initially realize an inner component with outer grooves where the tendon is wound and successively cast a second layer of polymer [6]. Yet, employing grooves does not guarantee disengagement of the tendon from its route during the second casting stage, and it requires generating individual molds for each combination of tendon routes that might need testing. Multi-step casting is also time-consuming and might generate delamination among successively cast polymer layers.

This work introduces a streamlined approach to fabricating tendon-driven soft actuators through a soft, 3D-printed endoskeleton, permitting single-step casting while eliminating the need for rigid inserts. The endoskeleton consists of hollow disks connected by slender arcs, through which flexible tubes guide the tendons. Its geometry is deliberately minimized to reduce interference with the actuator's deformation, while the use of a soft resin instead of rigid supports achieves a balance between uniform strain distribution at contact interfaces [11]

Received 30 April 2025; accepted 1 December 2025. Date of publication 25 December 2025; date of current version 12 January 2026. This article was recommended for publication by Associate Editor J. Hughes and Editor upon evaluation of the reviewers' comments. This work was supported in part by European Union - NextGenerationEU and in part by the Ministry of University and Research (MUR), National Recovery and Resilience Plan (NRRP), Mission 4, Component 2, Investment 1.5, project "RAISE - Robotics and AI for Socio-economic Empowerment" under Grant ECS00000035. *(Corresponding author: Emanuele Solfiti.)*

The authors are with the Istituto Italiano di Tecnologia, 16163 Genova, Italy (e-mail: emanuele.solfiti@iit.it; alessio.mondini@iit.it; deldot@sdu.dk; barbara.mazzolai@iit.it; alberto.parmiggiani@iit.it).

This article has supplementary downloadable material available at https://doi.org/10.1109/LRA.2025.3648604, provided by the authors.

Digital Object Identifier 10.1109/LRA.2025.3648604

IEEE Robotics and Automation Letters (RA-L) paper, presented at ICRA 2026, Vienna, Austria. Cite as RA-L paper.

and the resolution required for 3D printing. Once positioned in the mold, the structure remains embedded after curing, faithfully preserving the intended tendon path. The validity of the approach was assessed by comparing finite element (FE) simulations (performed without the soft endoskeleton) with experiments, which confirmed that the structure introduces only marginal effects on the achievable compliance.

II. Materials and Methods

A. Design and Fabrication

The problem is finding a robust, reproducible, and convenient way to fabricate a soft actuator that embodies the tendon accurately positioned along a given path. To address this problem, a 3D-printed endoskeletal structure is realized, composed of multiple disks connected by arcs, with the disks housing multiple holes or *eyelets* for the passage of the tendons. A key design criterion is the minimization of the impact on the actuator's overall deformation, and consequently its influence on the achieved deformed pose required for a potential task. As a case study, we designed a tendon-driven, silicone-based cylindrical actuator having 30 mm of diameter and 100 mm length. The design of the soft endoskeleton is generated through a semi-automatic process, split into two steps. The first step accounts for a Python script that takes as input the tendon path as a parametric curve in the 3D space:

$$\begin{cases} x = f(t) \\ y = g(t) \\ z = h(t) \end{cases} \quad t \in [0, 1],$$

a step of discretization g_i, a safety distance ε to keep between anchoring points and tendon, and a maximum arc slope $slope_{max}$ (Fig. 1). For simplicity of benchmarking, and because they capture the basic building blocks of most tendon routings, the tendon paths considered in this work are sigmoids of the type:

$$\vec{S}(t) = \begin{cases} x(t) = \frac{A}{1+e^{-kt}} \\ y(t) = 0 \\ z(t) = Ht - z_0 \end{cases} \quad t \in [-0.5, 0.5], \qquad (1)$$

where $A = 20\,\text{mm}$, $k = 50\,\text{mm}$, and $z_0 \in \{0, 25, -25\}$ mm. The selected parameters represent a compromise identified through iterative experimental optimization steps, trading between printing repeatability and structural integrity, and strictly depend on the material chosen for the fabrication and the actuator size.

The script outputs the sequence of points along the tendon route Q_i, the extremities of the arcs P_{ij}, and their middle points $\bar{P}_{ij}$. These, together with other geometrical parameters (Fig. 1), are input to the second step of the design procedure that automatically defines the endoskeleton geometry. Once the geometry is generated, manual inspection is carried out to correct possible overlaps. The process can be repeated to refine the initial parameter set, if desired. The software used for geometry generation is Grasshopper, a graphical algorithm editor integrated with Rhinoceros [12].

The simplified body and tendon geometry presented here were selected to facilitate explanation and visualization. However, the design and fabrication workflow can be generalized to more complex tendon paths and body shapes (see Supplementary Video), provided that the soft 3D-printed endoskeleton maintains the required flexibility.

A delicate design step is the curve discretization (Fig. 1): more discretization points (N) improve curve fidelity but also increase disk and arc density, which stiffens the actuator. We limited the gap to 10mm, to compromise between geometry fidelity and mechanical compliance.

At each discretization point, a flat disk is placed, connected by three rounded arcs with rectangular cross-sections ($b \times a = 1 \times 1.5$ mm). Arcs' geometry and positioning optimize symmetry and load distribution, while keeping a safety distance ε from tendon paths. Due to the chosen sigmoid shape, the routine positions the arcs at 120° each other (see Supplementary Video for a non-trivial case).

The final design steps involve placing the eyelets that serve as guides for both the tendons and the supporting wires while strengthening the structure along their crossing points. Supporting wires are used to center and hold the endoskeleton in position within the mold during the curing phase of the soft body. In the configuration shown, these wires were arranged both longitudinally, patterned at 120° intervals around the disks' axis of symmetry to constrain axial rotations, and radially, inserted across the disk's midplane, in a cross-like manner, to restrict longitudinal translation. Due to the reduced length and symmetrical design, only supports at the two extremities of the cylindrical actuator are required to stabilize the structure. The tendon is anchored at the disk N of the actuator via knotting it at a 3D-printed small rigid cylinder added to the endoskeleton (inset at the bottom right of Fig. 1). The endoskeleton is fixed to the mold before casting through the supporting wires, and it remains in the body at the end of the curing process, while the supporting wires are removed. Examples of how the endoskeleton is positioned in the mold are shown in Fig. 2, where the cases for producing the specimens for tensile and tendon pulling tests (described in Section II-B and II-C) are displayed.

The soft endoskeletons were printed using SLA technology on a Formlabs Form3 and Form4 (Formlabs, Somerville, MA, USA [13]) using Elastic 50 A resin [14], [15], a resin widely used to 3D print complex and highly deformable structures with fine details, such as lattices [16].

B. Tensile and Compression Tests

Tensile and compression tests were carried out to investigate whether the presence of an embedded 3D-printed structure could influence the mechanical response of the overall body under uniaxial stress conditions. Both types of test were performed on non-standard cylindrical specimens (see Figure 3) having the same dimensions as the cylindrical actuator described above except for the inclusion of larger extremities with 45 mm of diameter that served as clamping zones to prevent slippage caused by volume changes during tensile testing. Custom grips were 3D-printed to adapt the specimens to the used Universal Testing Machine (UTM, Zwick/Roell Z005 [17]). To fabricate the specimens, a closed mold was also 3D printed with a Formlabs Form3 using Black Resin V4 [18], as shown in the top part of Fig. 2. The material chosen was Ecoflex00-30 [19], a bi-component platinum-cured silicone largely used in soft robotics.

IEEE Robotics and Automation Letters (RA-L) paper, presented at ICRA 2026, Vienna, Austria. Cite as RA-L paper.

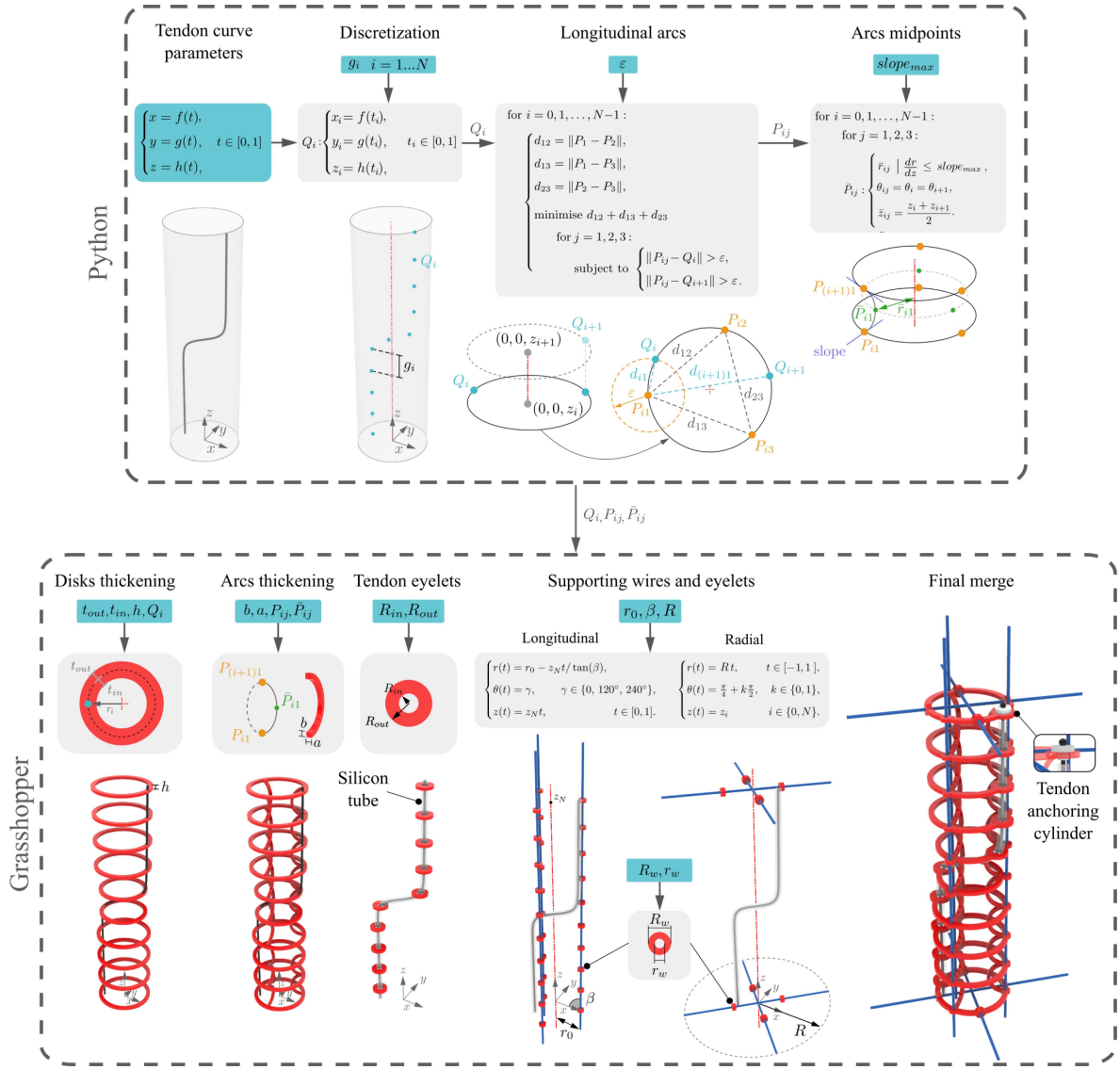

Fig. 1. Semi-automatic design process for the soft 3D-printed endoskeleton. The user inputs (light blue) a set of tendon curve parameters and constraints to a Python script, which discretizes the curves with target gap g to obtain the points Q. Longitudinal arcs are generated as circular arcs through pairs of points P, maximizing planar distance while ensuring a safety margin ε from Q; midpoints $\bar{P}$ are set by equalizing arc slopes. In a second stage, Grasshopper imports the Python outputs together with the geometrical parameters to build the solid model. Supporting wires (blue lines) are added for molding, with geometry largely independent of tendon paths, requiring adjustment only for major tendon or body shape changes.

This was cured for 4 hours after pouring as per the datasheet recommendations. A total of six specimens were tested: three without any internal structure and three incorporating different embedded structures, such as the ones at the top left in Fig. 3, without any embedded tendons. The structures were designed based on the criteria described in Section II-A, except for the number of disks, which were set to three, five, and nine, and for the omission of any tendon or supporting wire eyelet. The specimens were pulled at 1 mm/s in displacement control, up to 300% engineering strain, and compressed at the same speed up to 20% strain. The engineering stress-strain curves were plotted according to the following standard definitions:

$$\sigma = \frac{F}{A_0}, \quad \varepsilon = \frac{\Delta L}{L_0}$$

where F is the applied tensile force, $A_0 = \pi(D/2)^2$ is the initial cross-sectional area of the specimen, ΔL is the change in length during the test (negative in the compression case) and $L_0 = 100$ mm is the initial gauge length. It was noted that executing loading-unloading cycles up to 100% maximum tensile strain did not lead to any significant change in the curves, while cycling at higher peak stresses led to a curve stabilization after a few cycles, in agreement with experimental data shown in literature [20]. The tensile data reported here were therefore obtained at the third loading cycle.

C. Tendon Pulling Tests

Tendon-pulling tests can indirectly give information on the accuracy of tendon path reconstruction within the soft body

IEEE Robotics and Automation Letters (RA-L) paper, presented at ICRA 2026, Vienna, Austria. Cite as RA-L paper.

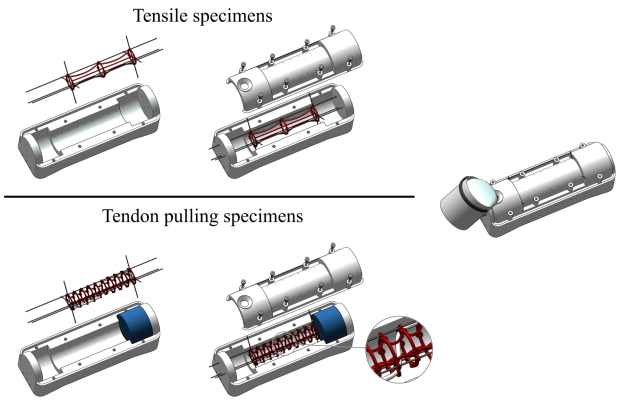

Fig. 2. Fabrication procedure for the tensile specimens (top part): after the placement of the endoskeleton and the mold closure, the silicone is poured through the inlet. The bottom part illustrates the fabrication procedure for the tendon-pulling specimens with one extremity of the mold occluded by a 3D printed cylinder (in blue). The structure is assembled with the longitudinal and radial supporting wires outside the mold. The wires are then tensioned and tightened to the mold, ensuring the structure maintains the desired configuration. The silicone is poured as before.

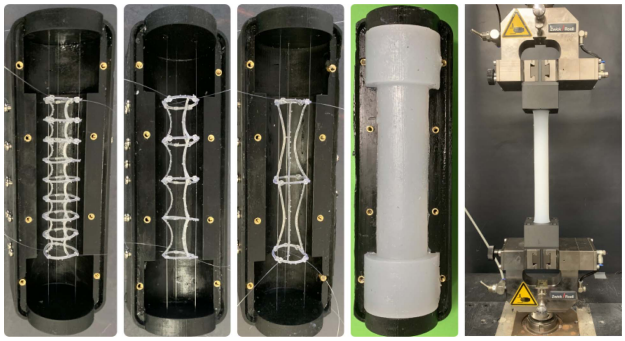

Fig. 3. Specimens fabrication with the three different embedded soft endoskeletons, and a frame captured during the tensile test.

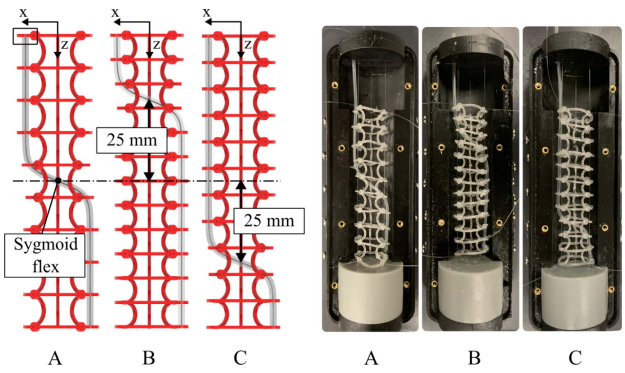

Fig. 4. Configurations A, B, and C of the sigmoid and the corresponding generated structures already placed in the mold before the pouring stage.

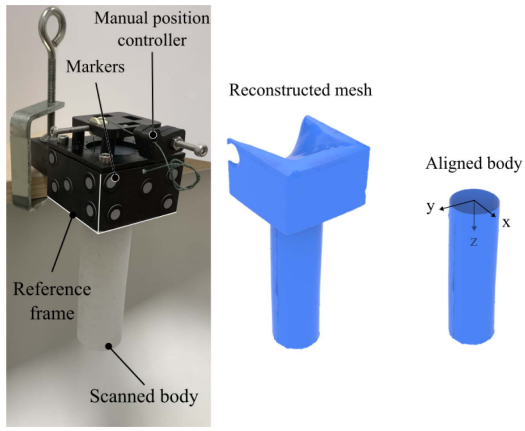

Fig. 5. 3D scanning setup and procedure. A reference frame was fit to the cubic specimen support and used for alignment with the FE simulations reference.

by checking whether pulling a specific tendon reproduces the predicted pose. To do so, FE simulations without any embedded structure were used as predicted pose and compared with real tests on specimens embedding the endoskeleton with the same sigmoid arrangements.

Three configurations, denoted as tests A, B, and C, were generated by simply shifting $z_0 = \pm 25$ mm in (II-A) as shown in Fig. 4. The fabrication process is described in the bottom part of Fig. 2: the procedure and mold are the same for each specimen, except for changing the structures designed to reconstruct each sigmoid. The same mold used for tensile specimens was adapted by sealing one extremity with a 3D-printed cylinder. A commercial fishing wire with a diameter of 0.2 mm was used to center and hold the endoskeleton in position as described in Section II-A. A silicone tube with internal and external diameters equal to 0.76 mm and 1.65 mm, respectively, is used to prevent sliding forces from damaging the surrounding silicone body during tensioning and unloading. A different commercial fishing wire from Spiderwire, Dura-4 Braid [21] with a diameter of 0.35 mm was used as tendon wire.

The pulling test consisted of pulling and holding the tendon at a fixed displacement parallel to the z axis and detecting the deformed pose using 3D scanning technique (EinScan HX from Shining 3D [22]). Each specimen was pulled up to 20, 30, 40, and 50 mm using a simple pulling system shown in Fig. 5. The specimens were scanned together with the cubic-shaped holder, and an STL mesh was reconstructed from the point cloud by using the software provided by the 3D scanner manufacturer. A reference frame was superposed to the holder by fitting a cuboid shape to the holder's flat faces and subsequently aligned to the FE simulation reference frame (see Section II-D) using a third software, i.e., Geomagic Design X [23]. A metric commonly used to evaluate the similarity between aligned point clouds is the Root Mean Squared Error ($RMSE$) [24]. This was used here to compare our 3D scanning data and simulation results. The calculation was performed in Python using the Open3D library [25] and consisted of the following steps:

- Extraction of FE nodes coordinates at 20, 30, 40, and 50 mm displacements of the pulling node,
- Uniform sampling of both the FE and scanned point clouds using the method `sample_points_uniformly`, with an equal number of points (50000),
- Computation of the distance d_i from each point in one point cloud to its nearest neighbour in the other, and vice versa, using the method `compute_point_cloud_distance`,

IEEE Robotics and Automation Letters (RA-L) paper, presented at ICRA 2026, Vienna, Austria. Cite as RA-L paper.

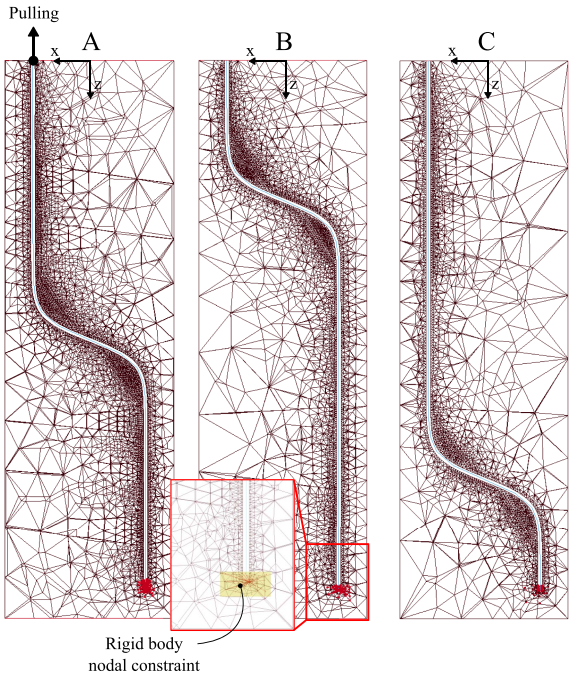

Fig. 6. Cross-section of simulated specimens with the three different configurations for the sigmoid. Here, the tendon channel is shown with the different shapes of the sigmoid.

TABLE I
MATERIAL PARAMETERS FOR CABLE MATERIAL MODEL

Density [g/cm^3]	Young's modulus [GPa]	Cross-sectional area [mm^2]
1	10	0.1

- Calculation of the $RMSE$ in both directions, as $RMSE = \sqrt{\frac{1}{n}\sum_{i=1}^{n} d_i^2}$, and selection of the maximum of the two.

D. Simulations

The FE models were realized with ANSYS LS-DYNA (ANSYS, Inc.) [26] using the explicit solver for the tendon-pulling simulations. Meshing was done in ANSYS APDL and post-processed with Python scripts. The three configurations A, B, and C of the sigmoid curve were generated, as shown in Fig. 6. The tendons were modeled using the material model *MAT_CABLE_DISCRETE_BEAM by setting the element formulation ELFORM = 6; these beam elements cannot withstand compressive loads, similar to real cable behaviors. The material parameters used are reported in Table I, and mass damping was imposed to limit the dynamic oscillation of the cable material model. The analytical curves were generated using (II-A), discretized with elements spanning a length of 1 to 4mm and having circular sections. The cross-sectional area was calculated from the real wire used in the experiments, and the Young's modulus and density were assumed to be reasonable values for general commercial fishing wires.The cylindrical body was meshed with tetrahedra (ELFORM = 13), known to better withstand large deformations. The material model adopted was the hyperelastic incompressible Ogden rubber model, a common choice for Ecoflex 00–30, with four series terms reported in Table II. The strain energy function for this material model is defined as:

$$W(\lambda_1, \lambda_2, \lambda_3) = \sum_{i=1}^{N} \frac{\mu_i}{\alpha_i} \left(\lambda_1^{\alpha_i} + \lambda_2^{\alpha_i} + \lambda_3^{\alpha_i} - 3\right)$$

where $N = 4$, μ_i and α_i are material constants and $\lambda_1, \lambda_2, \lambda_3$ are the principal stretches. The coefficients were obtained by fitting the stress-strain curves reported in Section III-A. The resulting curve was found to match well other datasets available for tension and compression of Ecoflex 00–30 in literature [20], [27], [28], [29].

TABLE II
MATERIAL PARAMETERS FOR HYPERELASTIC OGDEN RUBBER MODEL

	ρ [g/cm^3]	ν [-]	
	1.07	0.495	
μ_1 [MPa]	μ_2 [MPa]	μ_3 [MPa]	μ_4 [MPa]
0.1292	0.041 39	−0.5645	0.4354
α_1	α_2	α_3	α_4
7.762	1.3327	7.7883	7.7958

A circular channel with a diameter of 0.8 mm was swept and removed from the body to allow the tendon to slide inside. Element refinement was done around the channel, obtaining a fine mesh with a 0.5 - 1 mm characteristic length. A series of mesh-refining iterations suggested that the results were rather insensitive to the mesh size around the channel. Frictionless mortar contacts with viscous damping were used between the beams and the surrounding tetrahedra, and rigid body constraints were imposed at the anchoring node of the tendon with the surrounding body nodes. The nodes involved in the constraints were those falling within a cylindrical volume around the anchoring node, with a radius of 2 mm and a height of 4 mm (yellow region highlighted in Fig. 6), in analogy to the real anchoring system shown in Fig. 1.

The nodes at the cylinder base were all fixed along the z-axis direction, while the ones corresponding to the base perimeter were also fixed along the x and y axes. A simulation was performed for cases A, B, and C, pulling the tendon from 0 to 50 mm along the negative z-axis from the tendon end at the base of the cylinder. Before each simulation, a preliminary relaxation phase was performed to impose the gravity load while keeping the moving end fixed. This led to an overall deformation that shifted the nodes at the cylinder's free end by approximately 1 mm along z. To match the tendon-pulling tests, the deformed mesh coordinates were extracted at the pulling distances of 20, 30, 40, and 50 mm.

III. RESULTS

A. Tensile and Compression Tests

The results of the mechanical tests are shown in Fig. 7, which represents the engineering stress-strain curves for the various test conditions. The fitting curve obtained with the parameters of Table II accurately reproduces the experimental response across

IEEE Robotics and Automation Letters (RA-L) paper, presented at ICRA 2026, Vienna, Austria. Cite as RA-L paper.

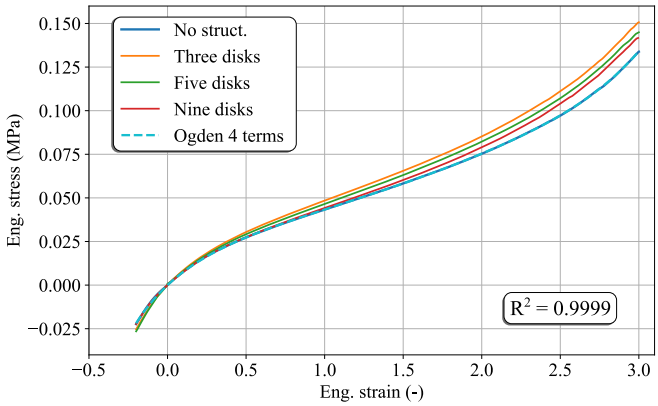

Fig. 7. Engineering stress-strain curves for non-standard Ecoflex 00–30 specimens with and without the soft endoskeleton. The results from the three specimens without any structure inside were averaged. The fitting parameters for the Ogden model are reported in Table II and were obtained from the fitting of specimens without any structure inside.

both the tensile and compressive strain domains. Decreasing the number of disks leads to a stiffening effect of the specimen under tension, i.e., a higher stress at the same strain. The same effect is not as clear in the negative strain domain, where the curves overlap without any trend.

B. Tendon Pulling Tests

The points of the meshes for each case, i.e., A, B, and C, reconstructed with the 3D scanning software, are reported in Fig. 8. The FE meshes extracted at the state corresponding to a displacement of the pulling node equal to 20, 30, 40, and 50 mm and aligned with the 3D scanning reference are superposed in the same figure. The visual match is rather satisfactory for most of the test cases, although the $RMSE$ is observed to increase with larger displacements. In test A, the deformed pose shows a double curvature and a flex located at the specimen's central section due to its sigmoid configuration. A slightly larger difference is visible in the second state, where the curvature closer to the tip is not perfectly reproduced. When the pulling node displacement is increased to 40 and 50 mm, the mismatch is fully recovered, and the $RMSE$ stabilizes around 1.5mm. For test B, the profile curvature progressively deviates from the simulation at increasing pulling displacement where the $RMSE$ overcomes 3 mm. The specimen shows a very small curvature radius at 50 mm, and folds become obvious on its ventral side skin. Test C shows good matching at all pulling displacements, but still featuring an increasing trend of the $RMSE$.

IV. Discussion

From the fabrication point of view, it is underlined that Elastic 50 A was used for our case study due to its ease of use and high success rate in 3D printing. It is not excluded that different 3D printing materials with similar properties, such as Formlabs Silicon 40 [30], Flexible 80A [31], or Stratasys Agilus 30 [32], would serve at the same scope with improved performances. The latter, for example, has a lower hardness value and soluble supports, which may greatly speed up the cumbersome phase of support removal. Similar reasoning could be used to choose the geometric parameters of the endoskeleton, which strongly depend on the tendon curve and soft body shape.

The stiffening effect seen in the positive strain domain of the tensile tests is not unexpected, considering that the stiffness of the Elastic 50 A is in the order of 1 MPa (see e.g. the Young's modulus at low strain measured in [33]), at least ten times higher than the value of the tangent slope calculated here at the origin ($\sim$ 0.09MPa). However, the volume fraction occupied by the structure ranges from 0.009 to 0.018, increasing with the number of disks, and a simplified rule of mixtures for the elastic modulus would give a very small contribution coming from the only material properties of the embedded structure. The critical role instead can be attributed to the longitudinal arcs that, when stretched, tend to align with the load direction. Increasing the number of disks leads to a decrease in the gap between them. Consequently, the corresponding $slope_{max}$ parameter can be increased to delay the alignment of the arcs with the load direction.

The FE simulations that predict the final arm poses intentionally exclude the embedded structure. Therefore, the good agreement between simulations and tests suggests that the structure's overall stiffness contribution to the final pose is low, though not fully negligible under certain conditions. In addition to reconstructing the pose predicted in the FE simulations, the tendon pulling tests served to analyze the specimens under a more complex state of stress, that is, a combination of tensile and compressive stresses, resulting from the buckling induced by the tendon. Plotting the minimum principal stress field for all tests (Fig. 9) at 50 mm pulling node displacement, it is visible that most of the elements undergo compressive stresses with a gradient towards tensile states at increasing distance from the tendon channel. Extreme deformations are achieved in the vicinity of the tendon channel where both compressive and tensile strain can overcome 100%. However, the average compressive strains developed within most of the elements of all the simulation specimens range around 50–70%. The mismatch between the poses predicted by the simulation and obtained in the test may be attributed to the internal endoskeleton disks that interact with the silicon: in particular, the portion of material included within the disk may constrain the degree of lateral expansion due to the Poisson's ratio at increasing compression strain. This is especially evident in test B, which also exhibits the highest compressive peak stresses on the ventral side of the specimen. In this case, the pose mismatch may be intensified by the gradual convergence of the disks, with the resulting folds acting as wedges and leading to a lower radius of curvature than predicted. In test A, since the flex is located halfway between the base and the tip, the compressive state is expected to be more uniformly distributed throughout the cylinder, and the overall deformation dominated by bending even at higher pulling-node displacements.

In test C, instead, compressive states become dominant at larger pulling-node displacements, and the mismatch with FE predictions increases in a manner similar to test B. These observations suggest that the influence of the soft endoskeleton becomes more pronounced when the stress state of the actuator

IEEE Robotics and Automation Letters (RA-L) paper, presented at ICRA 2026, Vienna, Austria. Cite as RA-L paper.

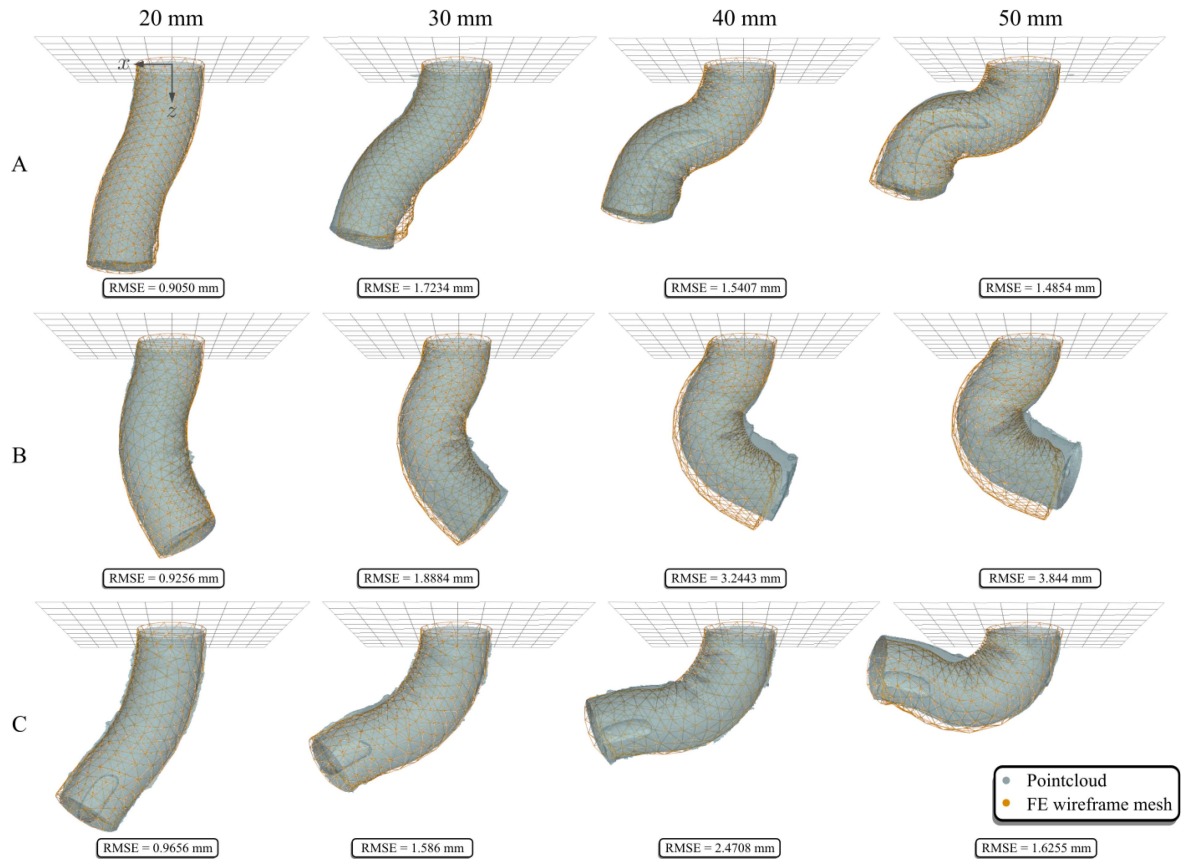

Fig. 8. Comparison of the simulated and scanned deformed states at 20, 30, 40, and 50 mm displacement of the pulling node. The FE meshes are shown in wireframe for clearer visualization. Below each test case, the resulting $RMSE$ is also given as a quantitative metric to assess the similarity of the FE nodes and 3D-scanned point clouds (lower is better).

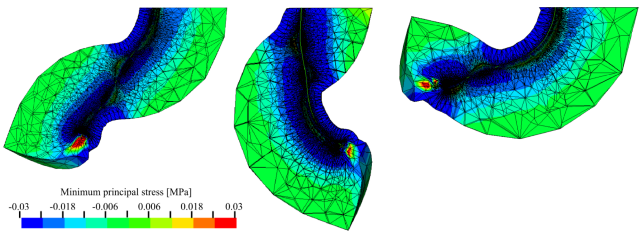

Fig. 9. Minimum principal stress field for tests A, B, and C, at 50 mm pulling distance (cross section). The principal stress distribution shows that the specimens are almost completely governed by compressive strains that move towards tensile states along with the distance from the tendon channel.

shifts from bending-dominated to compression-dominated states.

V. Conclusion

The proposed conceptual design can be considered an advantageous and promising solution for cable routing of nonlinear tendons embedded in soft bodies, which implies improved predictability and controllability of soft robots while easing tendon integration and fabrication of soft actuators. The topology of the structure is primarily designed for slender bodies, but can be extended to different body shape, provided the overall stiffness is not significantly compromised.

Unlike classical tendon-driven continuum robots, where the backbone and disks form the load-bearing structure that defines the manipulator's mechanical properties [34], [35], [36], in our design the internal 'disk + arcs' structure is entirely soft and intentionally non-structural: it provides only tendon routing and spacing, while the mechanical behavior is governed solely by the surrounding silicone body. The quantification of the stiffening led by the embedded structure is strictly related to the choice of the geometry and the stress state induced by the tendon arrangement. In our study, the constraining effect of the disks under compressive loading applied during the pulling tests may have affected the specimen's lateral deformation, and it was reflected in the mismatch between the real and FE predicted pose. Potentially, further optimization of the structure geometrical parameters and materials employed for the soft endoskeleton, or different choice of tendon trajectories and specimen shape could decrease or eliminate the stiffening effect, as well as refine the pose reproduction.

Acknowledgment

This work is part of the "Technologies for Sustainability" Flagship program of Istituto Italiano di Tecnologia (IIT).

The innovation described is the subject of a pending patent application to the Italian Patent Office with the title *Dispositivo robotico continuo* and Application Number 102025000008841.

IEEE Robotics and Automation Letters (RA-L) paper, presented at ICRA 2026, Vienna, Austria. Cite as RA-L paper.

REFERENCES

[1] D. Rus and M. T. Tolley, "Design, fabrication and control of soft robots," *Nature*, vol. 521, no. 7553, pp. 467–475, 2015.

[2] C. Laschi, B. Mazzolai, and M. Cianchetti, "Soft robotics: Technologies and systems pushing the boundaries of robot abilities," *Sci. Robot.*, vol. 1, no. 1, 2016, Art. no. eaah3690.

[3] W. Dou, G. Zhong, J. Cao, Z. Shi, B. Peng, and L. Jiang, "Soft robotic manipulators: Designs, actuation, stiffness tuning, and sensing," *Adv. Mater. Technol.*, vol. 6, no. 9, 2021, Art. no. 2100018.

[4] F. Schmitt, O. Piccin, L. Barbé, and B. Bayle, "Soft robots manufacturing: A review," *Front. Robot. AI*, vol. 5, 2018, Art. no. 84.

[5] V. Vikas, E. Cohen, R. Grassi, C. Sözer, and B. Trimmer, "Design and locomotion control of a soft robot using friction manipulation and motor–tendon actuation," *IEEE Trans. Robot.*, vol. 32, no. 4, pp. 949–959, Aug. 2016.

[6] J. Choi, S. H. Ahn, and K. J. Cho, "Design of fully soft actuator with double-helix tendon routing path for twisting motion," in *Proc. IEEE Int. Conf. Intell. Robots Syst.*, 2020, pp. 8661–8666.

[7] M. Calisti et al., "Study and fabrication of bioinspired octopus arm mock-ups tested on a multipurpose platform," in *Proc. 3rd IEEE RAS EMBS Int. Conf. Biomed. Robot. Biomechatronics*, 2010, pp. 461–466.

[8] B. Mazzolai et al., "Octopus-inspired soft arm with suction cups for enhanced grasping tasks in confined environments," *Adv. Intell. Syst.*, vol. 1, 2019, Art. no. 1900041.

[9] M. Manti, T. Hassan, G. Passetti, N. D'Elia, C. Laschi, and M. Cianchetti, "A bioinspired soft robotic gripper for adaptable and effective grasping," *Soft Robot.*, vol. 2, no. 3, pp. 107–116, 2015.

[10] P. Zhang, W. Chen, and B. Tang, "From two-dimensional to three-dimensional: Diversified bending modality of a cable-driven actuator and its grasping characteristics," *Soft Robot.*, vol. 9, no. 6, pp. 1154–1166, 2022.

[11] Z. Xie et al., "Octopus-inspired sensorized soft arm for environmental interaction," *Sci. Robot.*, vol. 8, no. 84, 2023, Art. no. eadh7852.

[12] "Grasshopper - Algorithmic modeling for Rhino," Accessed: Feb. 04, 2025. [Online]. Available: https://www.grasshopper3d.com/

[13] Formlabs, "High resolution SLA and SLS 3D printers for professionals," Accessed: Mar. 27, 2025. [Online]. Available: https://formlabs.com/

[14] "Elastic 50 A resin V1 - FormLabs," Accessed: Mar. 27, 2025. [Online]. Available: https://formlabs.com/store/materials/elastic-50a-resin-v1/

[15] "Elastic 50 A resin V2 - FormLabs," Accessed: Sep. 24, 2025. [Online]. Available: https://formlabs.com/store/materials/elastic-50a-resin-v2/

[16] S. Nakarmi, J. Kim, L. B. Bezek, J. A. Leiding, K.-S. Lee, and N. P. Daphalapurkar, "The role of unit cell topology in modulating the compaction response of additively manufactured cellular materials using simulations and validation experiments," *Model. Simul. Mater. Sci. Eng.*, vol. 32, no. 5, Art. no. 055029, 2024.

[17] "Universal Testing Machines for Static Applications - ZwickRoell," Accessed: Apr. 24, 2025. [Online]. Available: https://www.zwickroell.com/products/static-materials-testing-machines/universal-testing-machines-for-static-applications/

[18] "Black resin V4.0 - FormLabs," Accessed: Mar. 28, 2025. [Online]. Available: https://formlabs.com/store/materials/black-resin-v4-1/

[19] Smooth-On, Inc., "Ecoflex 00-30 product information," Accessed: Mar. 27, 2025. [Online]. Available: https://www.smooth-on.com/products/ecoflex-00-30/

[20] Z. Liao, M. Hossain, X. Yao, R. Navaratne, and G. Chagnon, "A comprehensive thermo-viscoelastic experimental investigation of ecoflex polymer," *Polym. Testing*, vol. 86, 2020, Art. no. 106478.

[21] "Shop all durabraid series | SpiderWire," Accessed: Apr. 28, 2025. [Online]. Available: www.spiderwire.com

[22] "EinScan HX - EinScan," Accessed: Mar. 27, 2025. [Online]. Available: https://www.einscan.com/einscan-hx/

[23] 3D Systems, "Geomagic design X," Accessed: Mar. 28, 2025. [Online]. Available: https://www.3dsystems.com/software/geomagic-design-x

[24] Q. Xiao, X. Gao, Z. Zhang, Y. Zhang, Z. Xu, and K. Shi, "Research on train wheel point cloud registration algorithm based on key points by fusing super-4PCS and ICP," *Sci. Rep.*, vol. 15, no. 1, 2025, Art. no. 32156.

[25] Q.-Y. Zhou, J. Park, and V. Koltun, "Open3D: A modern library for 3D data processing," 2018, *arXiv:1801.09847*.

[26] ANSYS, Inc., "ANSYS LS-DYNA," Accessed: Mar. 27, 2025. [Online]. Available: https://www.ansys.com/products/structures/ansys-ls-dyna

[27] J. L. Sparks et al., "Use of silicone materials to simulate tissue biomechanics as related to deep tissue injury," *Adv. Skin Wound care*, vol. 28, no. 2, pp. 59–68, 2015.

[28] D. Steck, J. Qu, S. B. Kordmahale, D. Tscharnuter, A. Muliana, and J. Kameoka, "Mechanical responses of Ecoflex silicone rubber: Compressible and incompressible behaviors," *J. Appl. Polym. Sci.*, vol. 136, no. 5, 2019, Art. no. 47025.

[29] L. Marechal, P. Balland, L. Lindenroth, F. Petrou, C. Kontovounisios, and F. Bello, "Toward a common framework and database of materials for soft robotics," *Soft Robot.*, vol. 8, no. 3, pp. 284–297, 2021.

[30] "Silicone 40 A resin - FormLabs," Accessed: Apr. 30, 2025. [Online]. Available: www.formlabs.com/uk/store/materials/silicone-40a-resin/

[31] "Flexible 80 A resin - FormLabs," Accessed: Apr. 30, 2025. [Online]. Available: www.formlabs.com/uk/store/materials/flexible-80a-resin/

[32] "Agilus 30 - Stratasys," Accessed: Apr. 30, 2025. [Online]. Available: www.stratasys.com/en/materials/materials-catalog/polyjet-materials/agilus30/

[33] M. V. Martire et al., "Measuring mechanical properties of 3D printed specimens for creating cerebral aneurysm mock-ups for surgical training," in *Proc. 2024 IEEE Int. Symp. Med. Meas. Appl.*, 2024, pp. 1–6.

[34] J. Starke, E. Amanov, M. T. Chikhaoui, and J. Burgner-Kahrs, "On the merits of helical tendon routing in continuum robots," in *Proc. 2017 IEEE/RSJ Int. Conf. Intell. Robots Syst.*, 2017, pp. 6470–6476.

[35] M. Russo, S. Wild, X. Dong, and D. Axinte, "Helical routing: Decoupling segments of tendon-driven continuum robots," *IEEE/ASME Trans. Mechatron.*, vol. 30, no. 3, pp. 2257–2269, Jun. 2025.

[36] M. Russo et al., "Continuum robots: An overview," *Adv. Intell. Syst.*, vol. 5, no. 5, 2023, Art. no. 2200367.

Open Access provided by 'Istituto Italiano di Tecnologia' within the CRUI-CARE Agreement